Investigating mechanical enhancement and vibrational response of additive manufactured PLA scaffolds with carbon nanotube and graphene oxide

Fabrication and multi-scale simulation

Angili, Sajad Niazi; Morovvati, Mohammadreza; Vatandoust, Yashar; Fotouhi, Mohammad; Bodaghi, Mahdi

DOI
10.1016/j.compstruct.2025.119320

Publication date
2025

Document Version
Final published version

Published in
Composite Structures

Composite Structures 369 (2025) 119320

Contents lists available at ScienceDirect

Composite Structures

journal homepage: www.elsevier.com/locate/compstruct

Investigating mechanical enhancement and vibrational response of additive manufactured PLA scaffolds with carbon nanotube and graphene oxide: Fabrication and multi-scale simulation

Sajad Niazi Angili [a], Mohammadreza Morovvati [a], Yashar Vatandoust [b], Mohammad Fotouhi [c,*], Mahdi Bodaghi [d]

[a] Department of Mechanical Engineering, Amirkabir University of Technology, 424 Hafez Ave., Tehran, Iran
[b] Department of Manufacturing and Production Engineering, University of Tabriz, Tabriz, Iran
[c] Faculty of Civil Engineering and Geosciences, Delft University of Technology, Delft, the Netherlands
[d] Department of Engineering, School of Science and Technology, Nottingham Trent University, Nottingham NG11 8NS, UK

ARTICLE INFO

Keywords:
3D-printing
Composite filaments
Scaffolds
Multi-scale simulations
Mechanical properties
Vibrational properties

ABSTRACT

This paper investigates the relationship between nanomaterials concentration, scaffold topologies, and mechanical and vibrational performance of additive manufactured Polylactic Acid (PLA) scaffolds reinforced with Graphene Oxide (GO) and Carbon Nanotube (CNT). Three different scaffold topologies namely Cube, Diamond, and Lattice Diamond were designed. Every scaffold comprised PLA reinforced with GO and CNT at different concentration levels of 0 wt%, 0.2 wt%, 0.4 wt%, and 0.6 wt%. The mechanical performance of scaffolds was evaluated via compressive testing. A representative volume element (RVE) model, evaluated using periodic boundary conditions, was developed and successfully validated against experimental results, with a deviation between 13.5 % to 23 %. The novelty of the work lies in incorporating GO and SWCNT agglomeration within the RVE models, enabling a more accurate comparison with 3D-printed composite test samples. Additionally, a comprehensive evaluation of scaffold shapes, geometry, vibrational response, and reinforcement concentration, provides valuable insights into their performance. Experimental and RVE results indicated that the PLAs reinforced with 0.6 wt% GO and 0.6 wt% CNT experience agglomerations. Finite element simulations using the Mooney-Rivlin hyperelastic model showed that the compressive strength of the structures followed this order: Diamond > Cube > Lattice Diamond. The results showed that increasing GO and CNT content from 0 wt% to 0.4 wt% led the Diamond scaffold to exhibit the greatest improvement in compressive strength and elastic modulus, with increases of 79.3 %, 26 %, 165.9 %, and 129 %, respectively. It was found that the additive manufactured modified PLA Diamond scaffold displays the best mechanical performance among the other scaffold topologies. The finite element analysis using the Lanczos Eigensolver revealed that mechanical enhancements and structural topology directly impact natural frequency variations, making them major parameters to consider for specific applications.

1. Introduction

Additive manufacturing (AM) technology provides a highly effective methodology for the construction of products with high levels of geometry complications without the need for new instruments [1]. AM is an emerging technology that can significantly alter the procedures and manufacturing operations in different sectors such as healthcare [2,3], transportation [4], energy [5] and other disciplines [6]. Additionally, AM can create structures from a diverse range of materials, such as metals [7], ceramics [8], and composites [9,10].

Fused deposition molding (FDM) is one of the most used AM approaches. FDM is the process of applying molten filaments layer-by-layer through an extrusion process. The molten blend material is dispensed on a platform after the mixtures are heated at the nozzle. Subsequently, the dissolved mixture of materials stack on top of the previous layers and consolidate into the ultimate forms [11]. The majority of thermoplastic polymers, powder/fiber composites, and metals are used as the material of choice for FDM [11]. Polymer filaments are

* Corresponding author.
E-mail address: M.Fotouhi-1@tudelft.nl (M. Fotouhi).

https://doi.org/10.1016/j.compstruct.2025.119320
Received 26 September 2024; Received in revised form 25 March 2025; Accepted 22 May 2025
Available online 24 May 2025

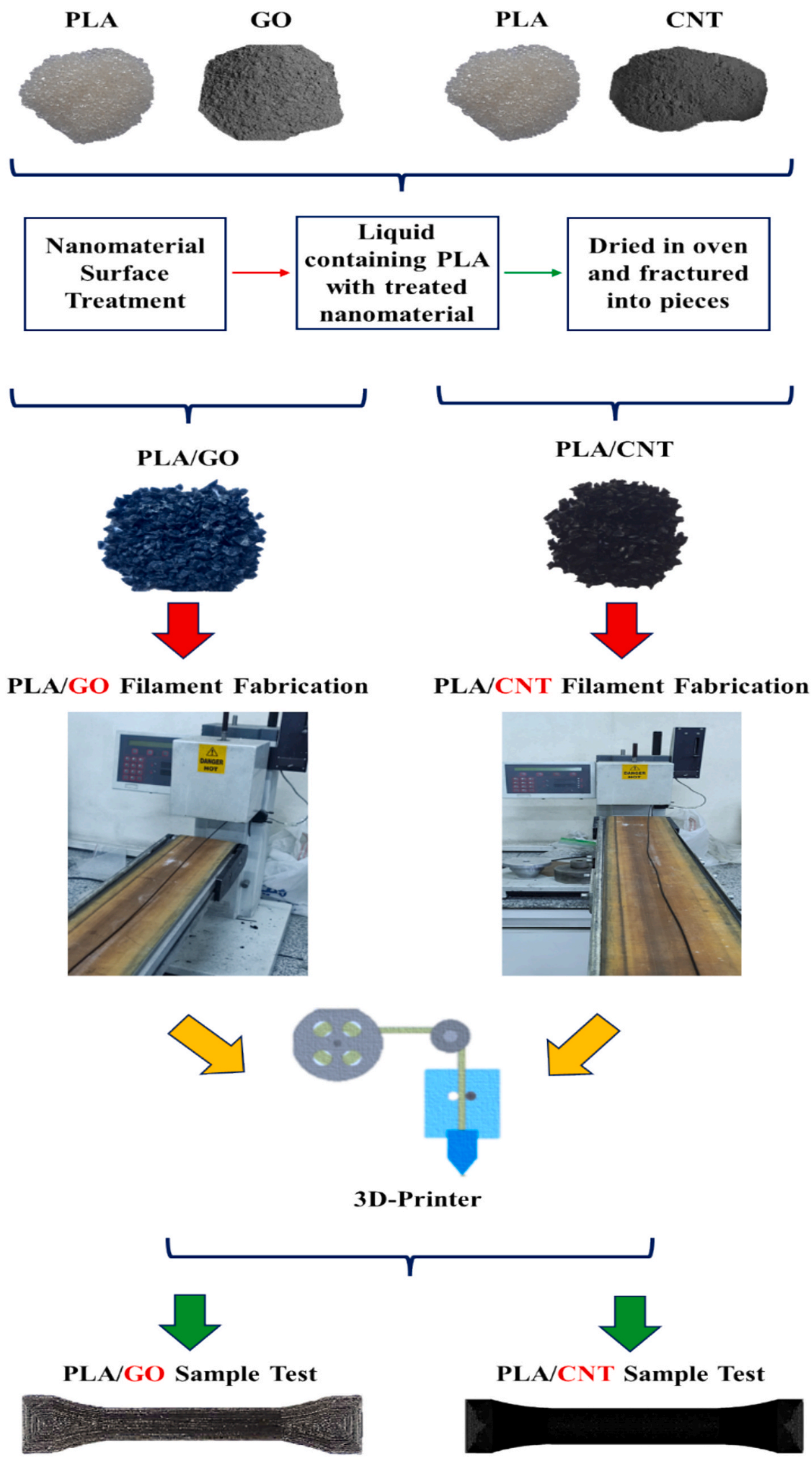

Fig. 1. Synthesized PLA/GO, and PLA/CNT particles for filament fabrication and Nanocomposite filament extruder machine.

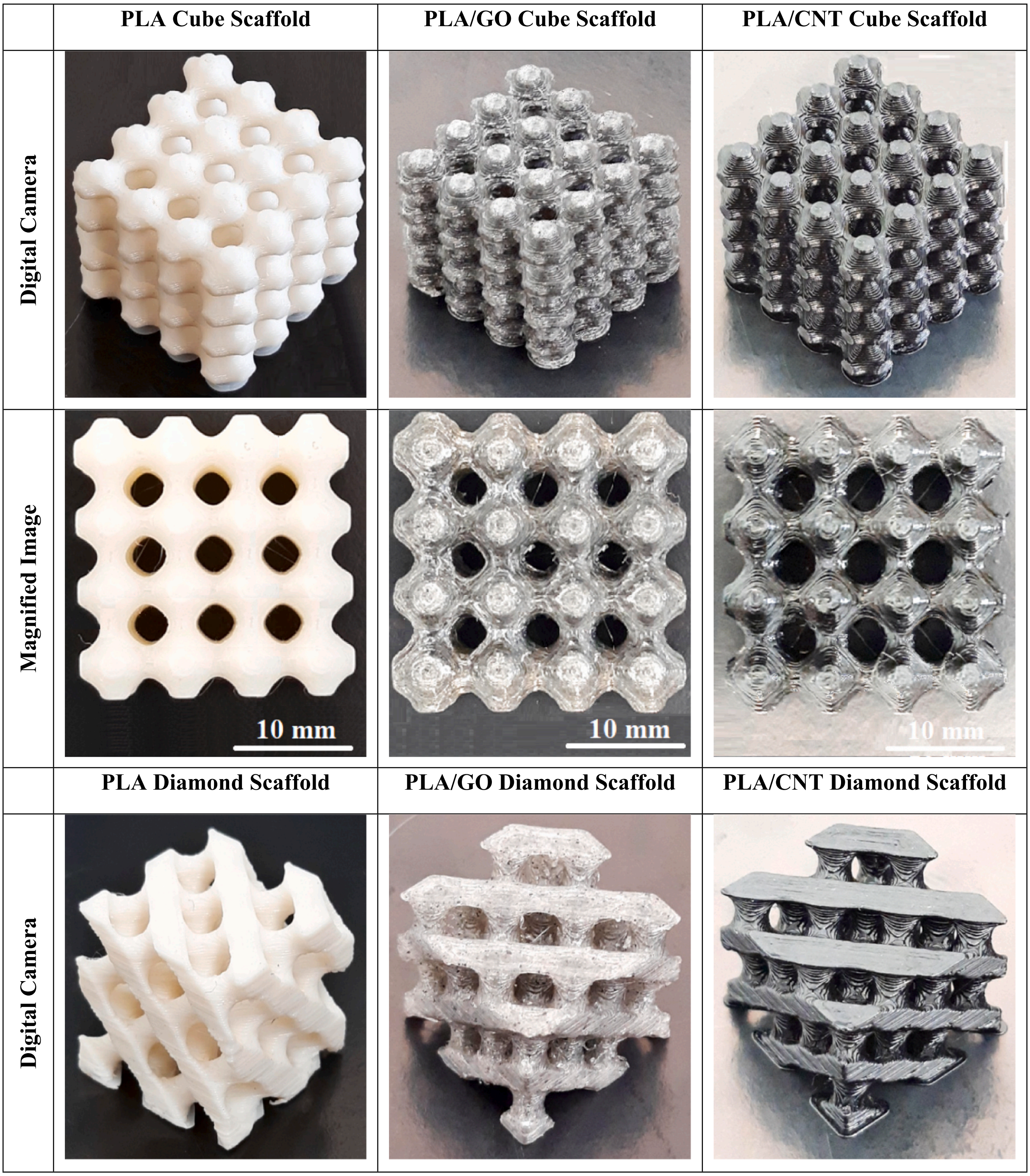

Fig. 2. Additively manufactured scaffolds, PLA, PLA/GO, and PLA/CNT.

utilized in the FDM process, which can be swiftly chilled to produce a wide variety of printed products and forms. The three-dimensional AM is capable of processing thermoplastic polymer materials, including acrylonitrile butadiene styrene (ABS) [12,13], PLA [14,15], polyamide (PA) [16], and polycarbonate (PC) [17], as well as thermosetting polymer materials like epoxies [18,19].

Recent years have seen a surge in the discussion regarding the creation of products with exceptional mechanical and physical performance for industrial applications, biomedical engineering, transportation, and other sectors, among other applications of AM [20–23]. For this purpose, a geometric model of the porous material is typically generated using computer-aided design software. This model is subsequently imported into the AM instruments in the form of STL files, and the model is subsequently processed with geometric segments and fabricated layer by layer [24]. In this line, a variety of structures and scaffolds have been developed, including honeycomb structures [25], porous lattice structures [26], mechanical metamaterials [27–29], plate-lattice scaffolds [30], diamond-based scaffolds [31], auxetic scaffolds [32], and triply periodic minimal surfaces (TPMS)-inspired scaffolds [33–36].

Due to its demand for eco-friendly, biocompatibility, and non-toxic degradation products, PLA has a broad range of applications from bone tissue regeneration to automotive applications such as jigs and fixtures [37,38]. Additionally, PLA is the most frequently employed

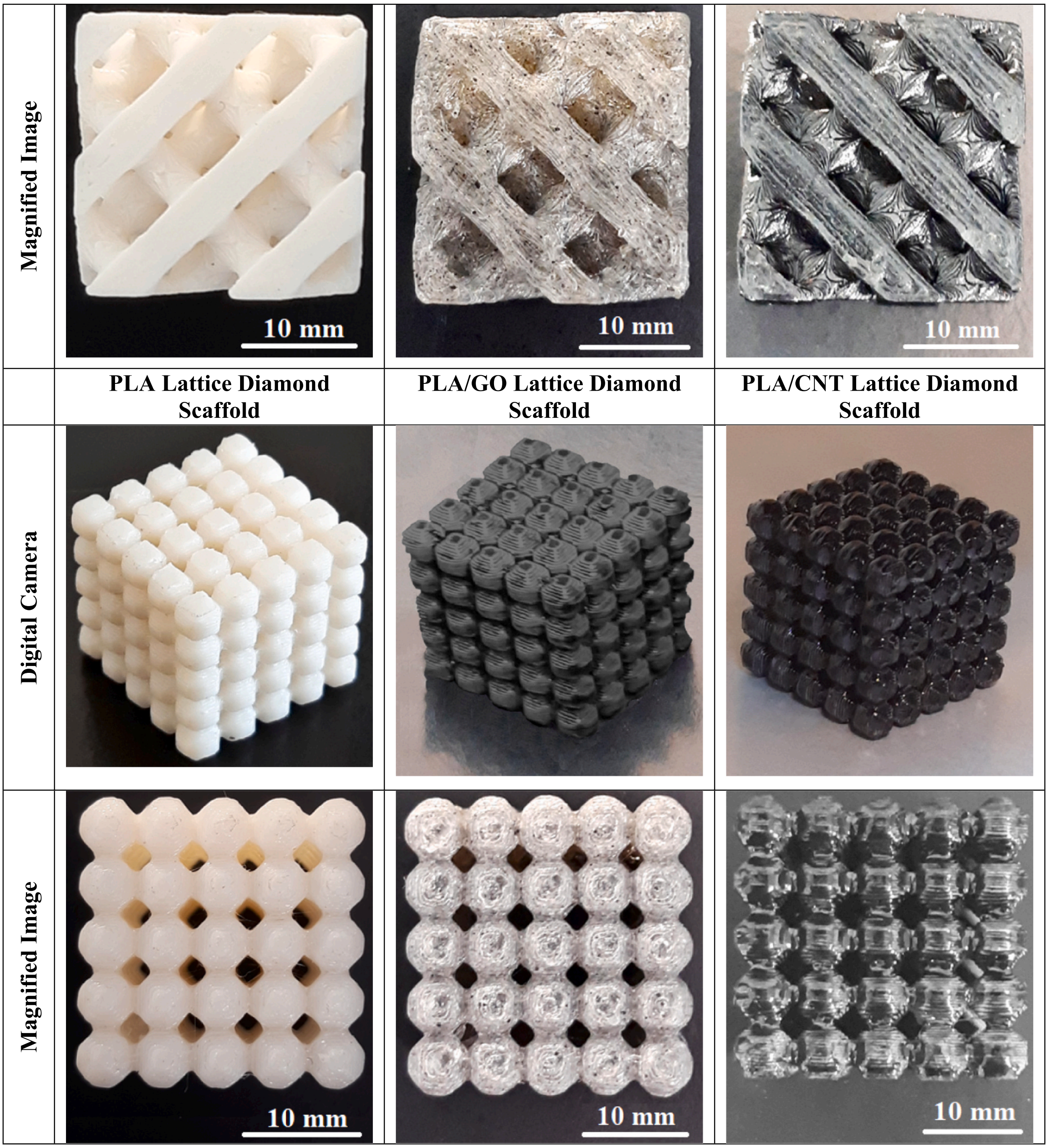

Fig. 2. (*continued*).

material in the FDM process for the production of certain medical devices, such as suture anchors, meshes, and fasteners [39]. The considerable modulus of elasticity, tensile strength, and limited elongation at fracture of PLA make it an appropriate material for use in bone tissue [40,41].

Nevertheless, additive manufactured PLA materials have limitations, such as mechanical strength in comparison to other materials [42]. It is crucial to take these limitations into account, particularly in applications that necessitate greater mechanical properties, despite their advantages [43,44]. In order to create AM products with desired properties, it is possible to combine reinforcements such as CNT, carbon fiber (CF), short glass fiber (SGF), short basalt fiber (SBF), and ceramic particles with the PLA matrix to create modified nanocomposite filaments [45–47].

PLA reinforced with graphene is one of the nanocomposites that are developed to overcome the neat PLA mentioned limitations [48–50]. The graphene network in the matrix has allowed composites to exhibit exceptional mechanical strength while preserving flexibility which is a consequence of the addition of graphene to the PLA matrix [51,52]. Research has been done to improve mechanical strength and enhance interfacial bonding between polymers and GO using surface modification agents, including sodium stearate [53], titanium ester coupling agents [54], and biomolecule L-lysine [55]. Pandey, Atul, et al. fabricated PLA reinforced with GO with high mechanical and surface properties using pencil lead for GO synthesization [56].

Moreover, PLA reinforced with CNT is one of the promising nanocomposites which can address the neat PLA drawbacks in recent years [57,58]. The extraordinary properties of CNT as nanofillers, such as a low density (1.3–2.0 g/cm3) and a high Young's modulus (0.3–1.0 TPa), have attracted significant attention [59,60]. As a result, these materials

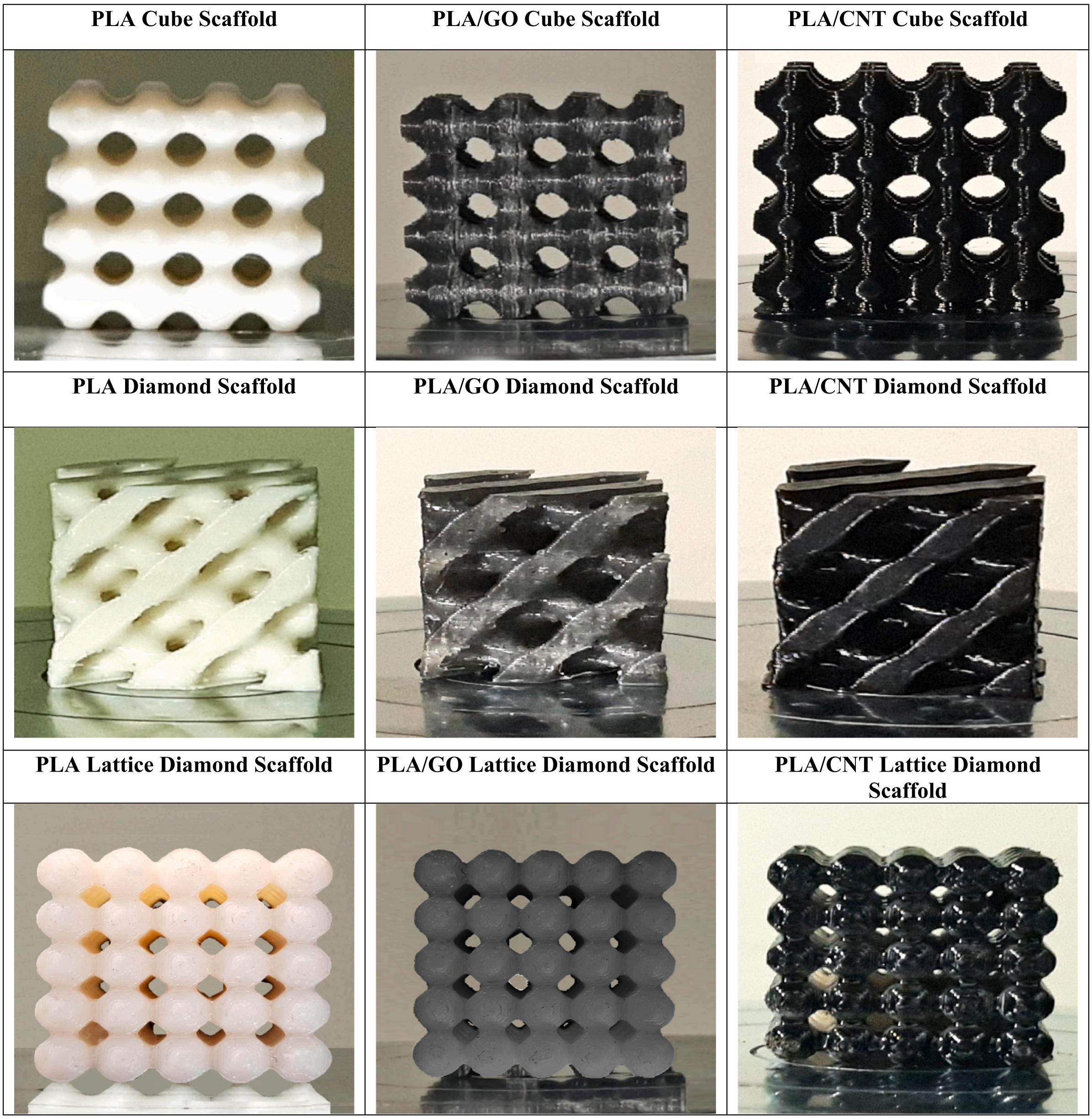

Fig. 3. Additively manufactured scaffolds under compressive test.

are both lightweight and durable. Furthermore, research suggests that CNT has the potential to be bioactive in biomedical applications, which could potentially enhance cell adhesion and proliferation, which are intriguing implementations of the PLA/CNT nanocomposite [50,61]. Additionally, the incorporation of CNTs into a PLA matrix can enhance the degree of crystallinity and crystallization process. The crystallization behavior of PLA mixed with multi-walled CNT was synthesized through melt blending [62]. The rapid spread and movement of PLA chains induce rapid heterogeneous crystallization due to CNT serving as an agent of nucleation [62].

Finite element method (FEM) has been used extensively to determine the most appropriate nanocomposite geometries with desired mechanical and physical characteristics such as elastic constants, compressive strength, and magnetic properties [63–65]. The numerical analysis results enable the researchers to acquire a more comprehensive and precise comprehension of the problem criteria prior to the commencement of the experimental process. The RVE is an appropriate method for the analysis of composites that contain two or more phases. The mechanical properties of the desired composites are predicted and supported by the appropriate representative volume element (RVE) model per their intended applications [66]. In composite materials theory, the RVE is the minimum volume at which a measurement may be obtained to provide a result that accurately represents the complete model [66]. The development of RVE models that integrate fibers and particles that are arbitrarily dispersed within the matrix is made possible by the DIGIMAT tool [67,68], which provides insights into complex materials' characteristics.

Existing literature reveals a gap in the systematic analysis of CNT-reinforced AM PLAs, particularly in evaluating scaffold architecture, material properties, and their interrelationships with mechanical performance [69,70]. This research addresses this gap by investigating various modified filaments and scaffolds to assess their mechanical properties, morphologies, and compressive load responses. The objective is to identify the optimal scaffold topology and nanomaterial composition for superior mechanical performance by comparing experimental results with finite element simulations. PLA reinforced with graphene oxide (GO) and CNT is used to fabricate three distinct 3D scaffold designs: Cube, Diamond, and Lattice Diamond. These scaffolds

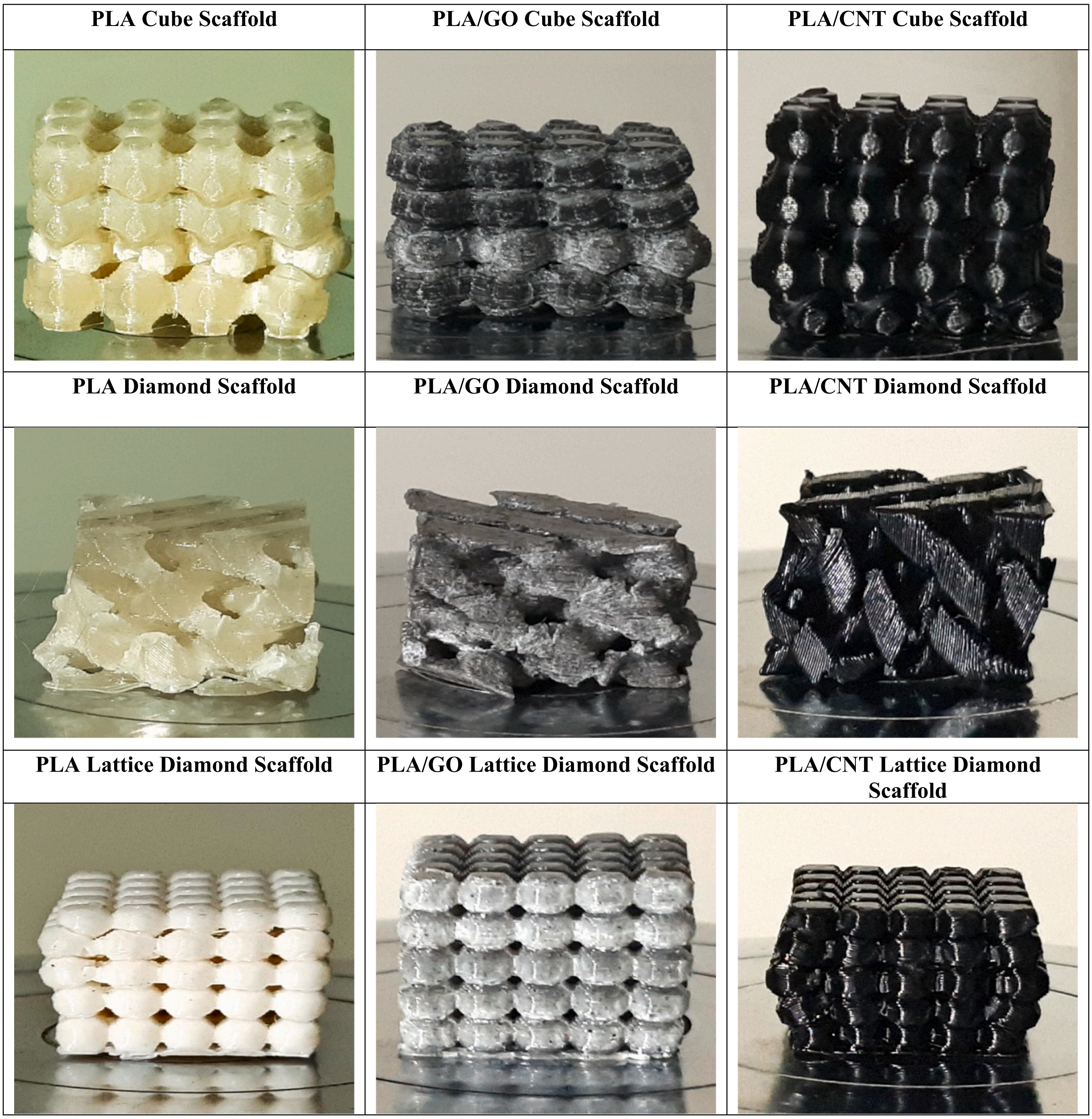

Fig. 4. Additively manufactured scaffolds, PLA, PLA/GO, and PLA/CNT after compressive test.

are analyzed for their mechanical performance and vibrational behavior to determine the influence of architecture and filament modifications.

Detailed microstructural analysis is conducted using FESEM to assess the dispersion and agglomeration of GO and CNT, and their impact on mechanical strength. Compressive testing is performed to evaluate the elastic modulus and compressive strength. Additionally, RVE is analyzed under periodic boundary conditions (PBC) to predict the material properties of the modified filaments. FEM is used to investigate the stress distribution and mechanical response of the scaffolds. To enhance accuracy, experimental testing of the scaffolds is performed to determine the Mooney-Rivlin hyperelastic constants. Moreover, to investigate the influence of mechanical enhancement and structure topologies on the vibrational response and identifying their resonance, natural frequency of structures was determined. Thus, a new perspective for choosing the appropriate structures for applications were provided. The following sections provide a detailed analysis of each of these aspects.

2. Materials and methods

At first, PLA/GO and PLA/CNT 3D printer filaments were manufactured. Subsequently, test samples were produced, and hyperelastic constants were ascertained. The scaffold models were generated and incorporated into the additive manufacture software (Simplify 3D) for the purpose of printing the scaffolds with modified filaments that were fabricated. Following this, FESEM was employed to examine the morphology and microstructure behavior of PLA, PLA/GO, and PLA/CNT nanocomposites. Additionally, scaffolds were subjected to compressive testing in order to assess their mechanical and physical characteristics. The subsequent subsections provide a comprehensive explanation of each of the aforementioned subjects.

2.1. Materials and filament preparation

Pure PLA granules (Sigma-Aldrich, Germany) were combined with a variety of nanomaterials to create a composite material: CNT (US Research Nanomaterials Inc., USA) treated with strong nitric acid, PBS

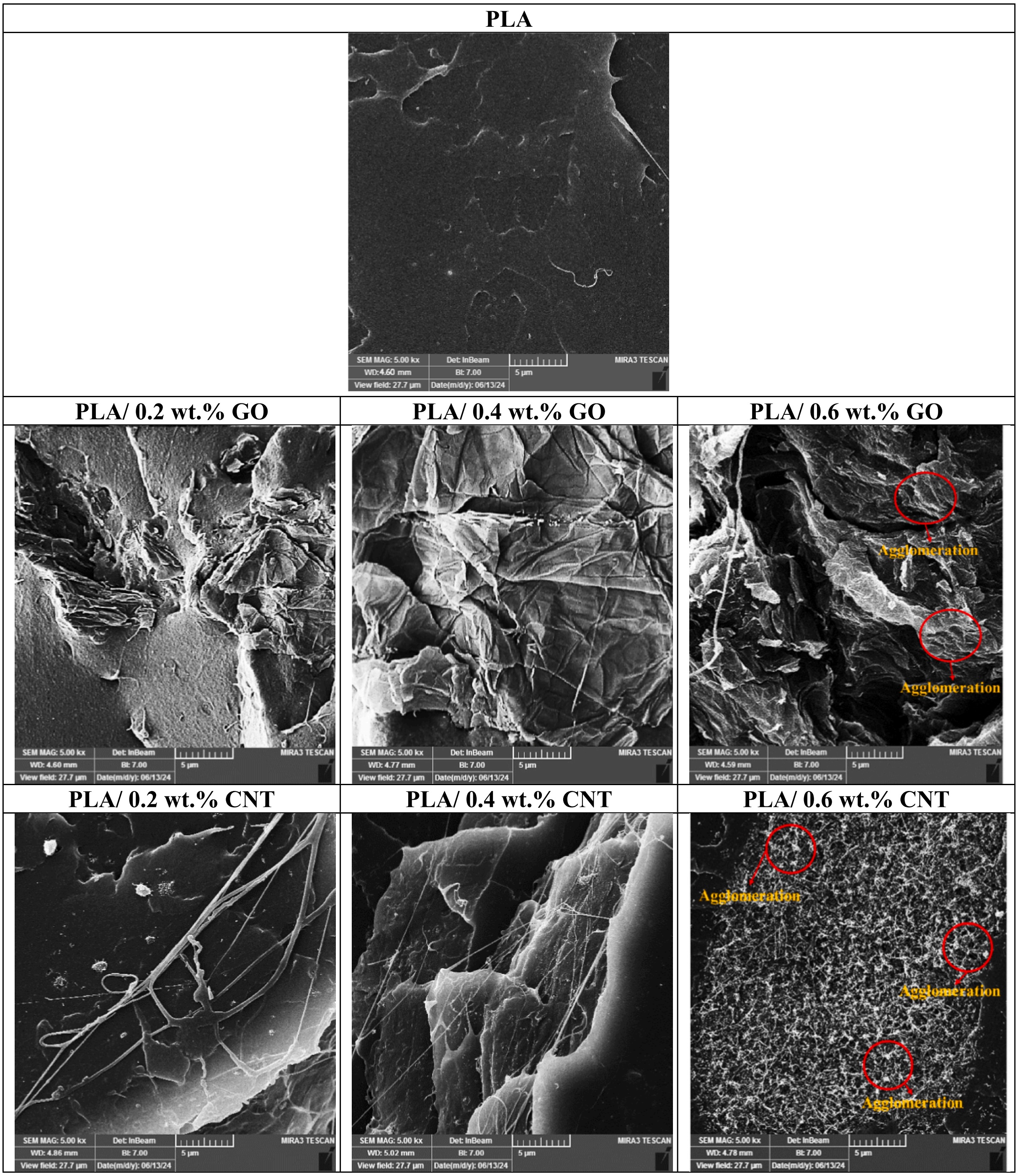

Fig. 5. Morphology and microstructure of the neat PLA, PLA mixed with 0.2 wt% GO (G1), PLA mixed with 0.4 wt% GO (G2), and PLA mixed with 0.6 wt% GO (G3), PLA mixed with 0.2 wt% CNT (C1), PLA mixed with 0.4 wt% CNT (C2), and PLA mixed with 0.6 wt% CNT (C3).

powder, introducing hydroxyl (–OH) and carboxyl (–COOH) groups onto their surface as surface treatment, and GO nanoplates (US Research Nanomaterials Inc., USA) prepared through mechanical stripping. The components were mixed for 10 min at a rotor speed of 60 r/min and a temperature of 150 °C using a Haake torque rheometer (Haake PolyLab OS) [71]. After being centrifuged, the liquid above the sediment was filtered, washed with deionized water, and dehydrated in an oven at 60 °C for one day. The solid that resulted was chilled and subsequently fractured into 0.5 cm-diameter fragments. The nanocomposite filament extruder machine and the synthesized particles for modified PLA filaments are depicted in Fig. 1. Moreover, PLA/GO and PLA/CNT particles were prepared for subsequent filament fabrication, as illustrated in Fig. 1.

Wire-shaped composites were produced to satisfy the precise specifications of the FDM 3D printer (Raise-3D Pro2 Plus) by meticulously managing the temperature and extruding composite particles through a small single-screw extruder. It is crucial to be aware that the extrusion temperature was contingent upon the specific composite formulation. The synthesis of PLA/GO and PLA/CNT nanocomposites was conducted using three different weight percentages: G1, G2, and G3, which consisted of PLA mixed with 0.2 wt% GO, 0.4 wt% GO, and 0.6 wt% GO, respectively. Additionally, C1, C2, and C3, which consisted of PLA

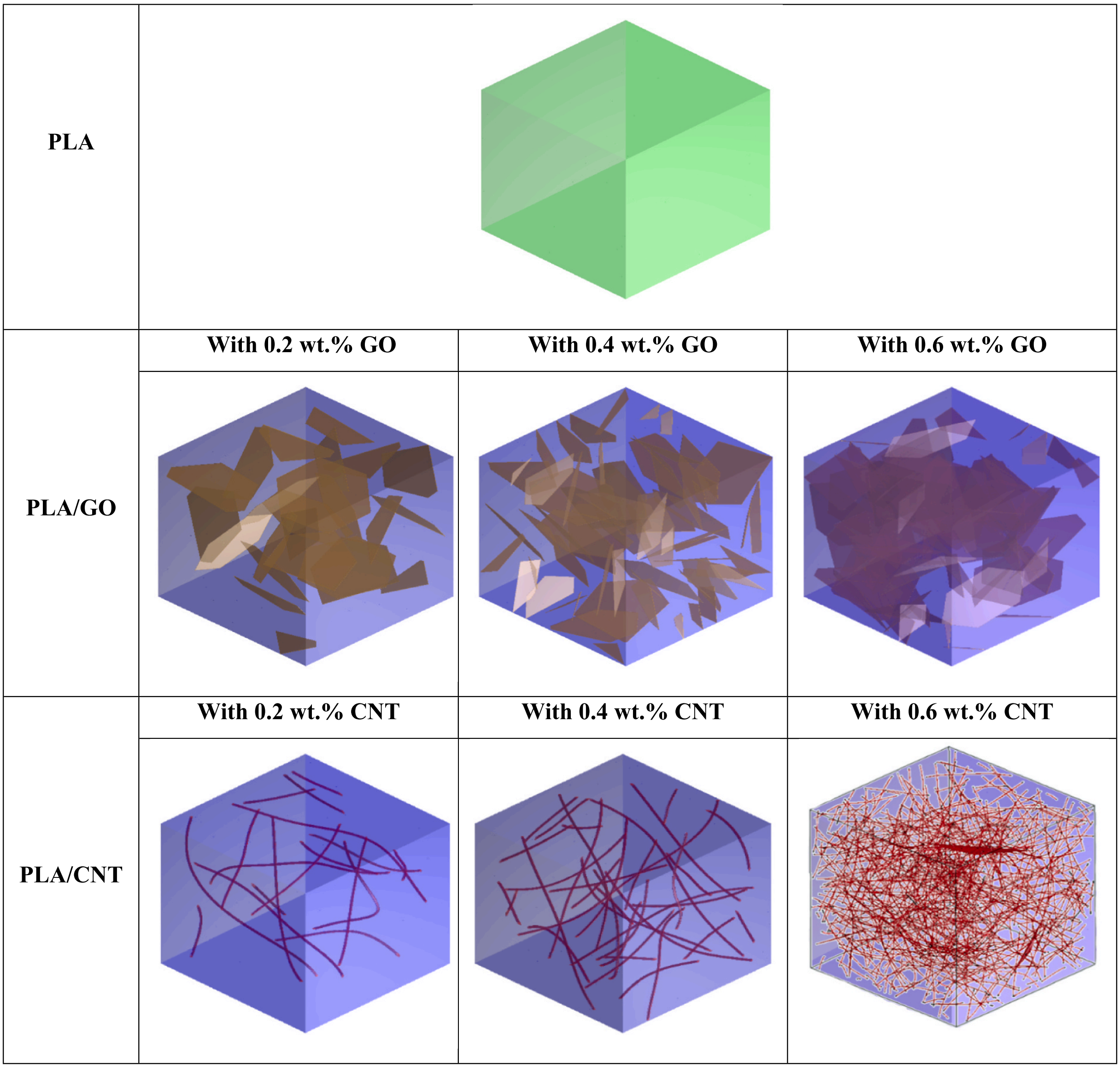

Fig. 6. Neat PLA, PLA mixed with 0.2 wt% GO (G1), PLA mixed with 0.4 wt% GO (G2), and PLA mixed with 0.6 wt% GO (G3), PLA mixed with 0.2 wt% CNT (C1), PLA mixed with 0.4 wt% CNT (C2), and PLA mixed with 0.6 wt% CNT (C3) RVEs.

mixed with 0.2 wt% CNT, 0.4 wt% CNT, and 0.6 wt% CNT, were also synthesized. Analysis of the mechanical characteristics of PLA, PLA/GO, and PLA/CNT was conducted utilizing test samples, which also yielded the essential data for a following FEM investigation.

2.2. Scaffolds printing

Three distinct structures (Cube, Diamond, and Lattice Diamond) are generated using CATIA software. The dimensions of each scaffold are 2.4 cm in length, 2.4 cm in width, and 2.4 cm in height. Additionally, the porosity ratio of the structure's ranges from 45 % to 55 %.

The corresponding STL files were generated by simplified 3D software as input after the associated design was completed. These files were evaluated for any required adjustments to the AM equipment. Rapid prototyping enables the immediate fabrication of systematically organized and biologically suitable scaffolds from a computer. FDM 3D printer (Raise-3D Pro2 Plus) has a speed range of 30–150 mm/s, a maximum nozzle temperature of up to 300 °C, and a variety of nozzle diameters, including 0.2 mm, 0.4 mm, 0.6 mm, 0.8 mm, and 1 mm. The temperature, nozzle diameter and filaments diameter were set to 210 °C, 0.4 mm, and 1.75 mm, respectively. Moreover, simulations were conducted to extract G-code and perform AM. The AM apparatus was subsequently programmed with the credentials that were acquired. The production phase commences following calibration, and each sample requires approximately three hours. The scaffolds that were additively manufactured are depicted in Fig. 2. Each scaffold was appropriately printed, and the quality of the architecture and porosity were satisfactory. Each scaffold in Fig. 2 is illustrated in two main perspectives, including an isometric view and a magnified view to visualize the scaffold geometry and structure.

2.3. Experimental procedures

The scaffolds were assessed for their mechanical and physical characteristics utilizing a compressive strength testing mechanism (SANTAM-STM50, Amirkabir University of Technology). Fig. 3 depicts the compressive test conducted on scaffolds produced by AM.

By subjecting each sample to a displacement rate of 0.2 mm/min, its compressive strength is evaluated. The stress–strain curve is generated by the output of the device, which includes data on displacement and

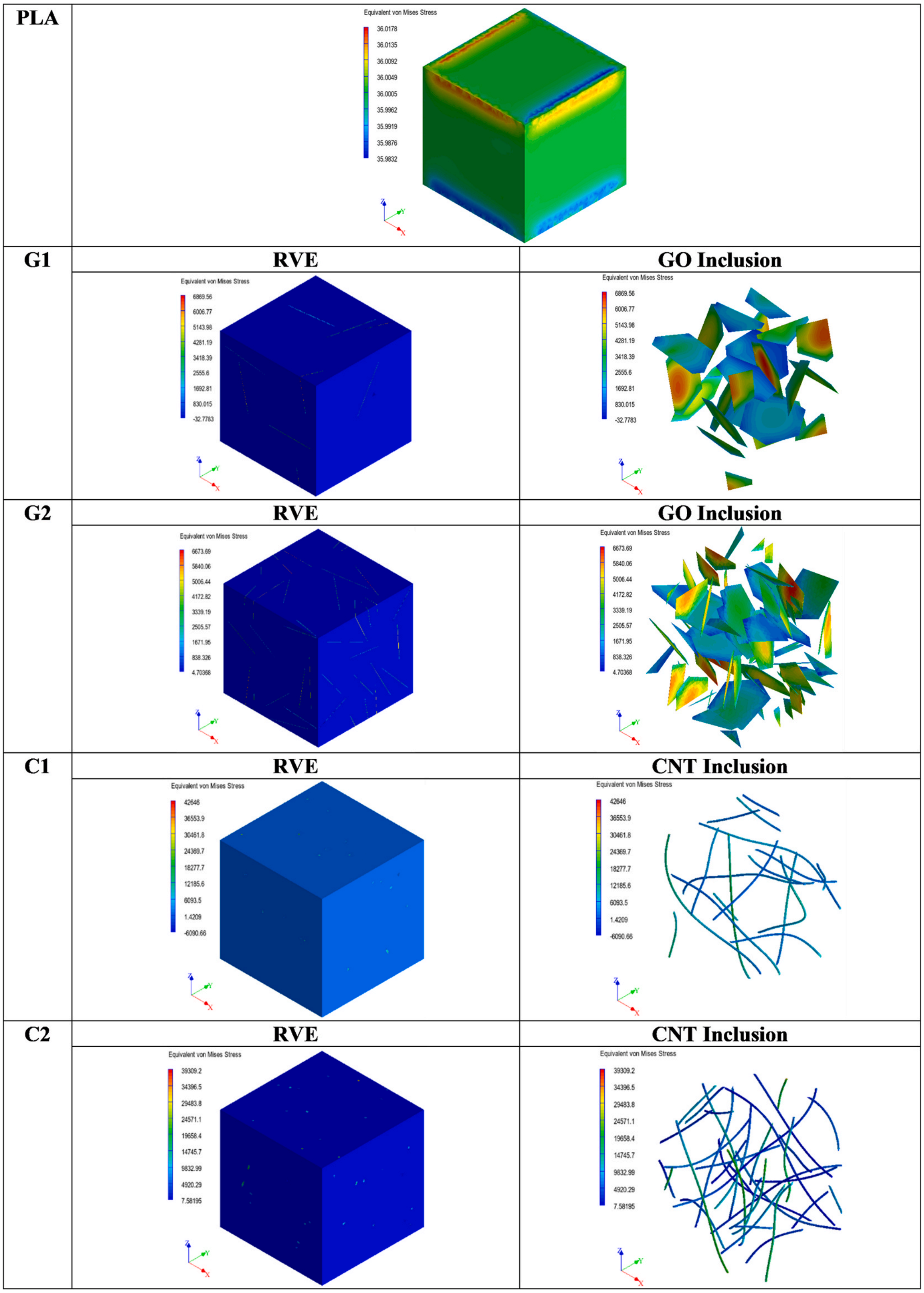

Fig. 7. Neat PLA, PLA mixed with 0.2 wt% GO (G1), and PLA mixed with 0.4 wt% GO (G2), PLA mixed with 0.2 wt% CNT (C1), PLA mixed with 0.4 wt% CNT (C2) Von Misses Equivalent Stress.

Table 1
Mechanical properties of PLA/CNT, and PLA/GO test samples obtained by RVE and EXP.

Sample	RVE		EXP		Error (%)
	Elastic Modulus (MPa)	Poisson Ratio	Elastic Modulus (MPa)	Poisson Ratio	
G1	1551.98	0.32	1338.12	0.33	13.78
G2	2128.02	0.31	1824.78	0.33	14.25
G3	1837.09	0.31	1493.81	0.32	22.98
C1	4494.27	0.33	3885.75	0.33	13.54
C2	5071.83	0.32	4287.22	0.32	15.47
C3	4323.23	0.32	3536.52	0.32	22.24

Table 2
Mooney-Rivlin constants c_{10} and..c_{01}

Sample	c_{10}(MPa)	c_{01}(MPa)
PLA	156	84
G1	182	89.64
G2	248.2	122.25
C1	528.52	260.32
C2	664.19	312.56

force. To calculate the elastic modulus of each sample, the gradient of the elastic area of the stress–strain curve was computed. Additionally, the microstructure of the scaffolds was examined using a FESEM (MIRA3, TESCAN, Germany) after they were coated with gold in a cold sputtering coater (Scd005, Leica, Czech Republic) at a voltage of 10 kV.

3. Multi-scale simulation

A multiscale analysis was conducted to examine the RVE of PLA/BN, PLA/GO, and PLA/CNT. The RVE model was examined under PBCs to attain satisfactory results. PBCs are a collection of constraints that are frequently implemented to simulate an infinitely large system through the utilization of a diminutive component known as a unit cell. PBCs are included in computer simulations and mathematical models. In contrast to experimental studies, this approach demonstrated the ability to accurately determine the mechanical characteristics of a wide range of nanocomposites. Subsequently, the generation of RVEs and the examination of test samples were discussed. Additionally, Abaqus software was employed to conduct FEMs to examine the mechanical properties of scaffolds. In order to guarantee mesh convergence and achieve consistent outcomes, a trial-and-error approach was implemented. As a result, the mesh size was taken to be 0.4 mm for all finite element simulations. The hyperelastic properties of the fabricated scaffolds were used to define the material properties. Simulations were conducted using the Mooney-Rivlin model. The strain energy function for the Mooney-Rivlin model was established using the following equation [72]:

$$U = C_{10}(\bar{I}_1 - 3) + C_{01}(\bar{I}_2 - 3) + \frac{1}{D_1}(J^{el} - 1)^2 \tag{1}$$

where C_{10}, C_{01}, and D_1 are material parameters. $\bar{I}_1$ and $\bar{I}_2$ are the first and second deviatoric strain invariants defined as:

$$\bar{I}_1 = \bar{\lambda}_1{}^2 + \bar{\lambda}_2{}^2 + \bar{\lambda}_2{}^2 \tag{2}$$

$$\bar{I}_1 = \bar{\lambda}_1{}^{(-2)} + \bar{\lambda}_2{}^{(-2)} + \bar{\lambda}_2{}^{(-2)} \tag{3}$$

where the deviatoric stretches $\bar{\lambda}_i = J^{-\frac{1}{3}}\lambda_i$($J$ is the total volume ratio), J^{el} is the elastic volume ratio, and λ_i are the principal stretches [73]. The formulae defining initial shear modulus (μ_0) and bulk modulus (K_0) are defined by following equations:

$$\mu_0 = 2(c_{10} + c_{01}) \tag{4}$$

$$k_0 = \frac{2}{D_1} \tag{5}$$

According to R. Afshar et al. [74], hyperelastic constants were obtained. In this study incompressible Mooney-Rivlin model was considered.

4. Results and discussions

4.1. Mechanical results

The mechanical performance of the scaffolds (PLA, PLA/GO, and PLA/CNT) was evaluated using compressive testing, as shown in Fig. 4. Buckling occurred in the Cube scaffolds due to the narrow links in their structure. In contrast, the Diamond scaffolds experienced link fractures, while the Lattice Diamond scaffold was uniformly compressed without collapsing or breaking. This behavior was primarily attributed to the absence of interconnected links in the Lattice Diamond design.

FESEM images of the PLA, PLA/GO, and PLA/CNT scaffolds are shown in Fig. 5. At 0.2 wt% and 0.4 wt% concentrations, CNT and GO nanomaterials were evenly dispersed within the PLA matrix, with no evidence of aggregation. On the other hand, scaffolds made with PLA reinforced with 0.6 wt% GO and 0.6 wt% CNT showed significant agglomeration, which could considerably weaken their overall mechanical strength.

4.2. Finite element results

The commercial DIGIMAT software platform (developed by e-Xstream Engineering SA) was used to construct the RVE models, incorporating DIGIMAT-FE as a practical tool. The nanomaterial weight percentages (GO and CNT) varied at 0 wt%, 0.2 wt%, 0.4 wt%, and 0.6 wt%. RVEs were generated by analyzing microstructure data, including Poisson's ratio, elastic modulus, and material density. GO in the RVE was modeled as nanoplates with diameters of 10–50 μm and a thickness of 7 nm, while CNTs were represented as curved cylinders with a diameter of 1 nm and an aspect ratio of 1000, based on the datasheet specifications (length = 1000 nm). The PLA/GO and PLA/CNT nanocomposites were synthesized in three different weight percentages: 0.2 wt% (G1), 0.4 wt% (G2), and 0.6 wt% (G3). GO and CNT nanomaterials were assumed to be elastic and isotropic, with random distribution within the PLA matrix during RVE simulations to enhance precision. Each RVE model underwent five tests to ensure the accuracy of the simulations, with the PLA, PLA/GO, and PLA/CNT RVEs shown in Fig. 6. Cluster formations were observed in RVEs with 0.6 wt% GO and CNT, potentially reducing mechanical properties, as indicated in Fig. 6. Therefore, the research proceeded with PLA reinforced with 0.2 wt% and 0.4 wt% GO and CNT.

The PBCs allow for the simulation of a microsystem without surface constraints or external forces, enabling it to reach uniformity at a larger scale. This approach is essential for examining RVEs, achieved through the periodic repetition of PBCs in all directions [67]. It allows for modeling a compact system without surface boundaries, facilitating the comparison and analysis of numerical results with experimental findings. Fig. 7 presents the equivalent stress for PLA, PLA mixed with 0.2 wt % GO (G1), and PLA mixed with 0.4 wt% GO (G2), as well as PLA mixed with 0.2 wt% CNT (C1) and PLA mixed with 0.4 wt% CNT (C2).

Table 1 presents the mechanical parameters of PLA/GO and PLA/CNT composites obtained through PBCs and experimental results. It can be seen that the elastic modulus determined using PBCs aligns well with experimental values, with an error margin ranging from 13.5 % to 23 %. The elastic modulus of PLA/GO increased from 1551.98 MPa (G1) to 2128.02 MPa (G2), as shown in Table 1. Similarly, the elastic modulus of PLA/CNT increased from 4498.27 MPa (C1) to 5071.83 MPa (C2).

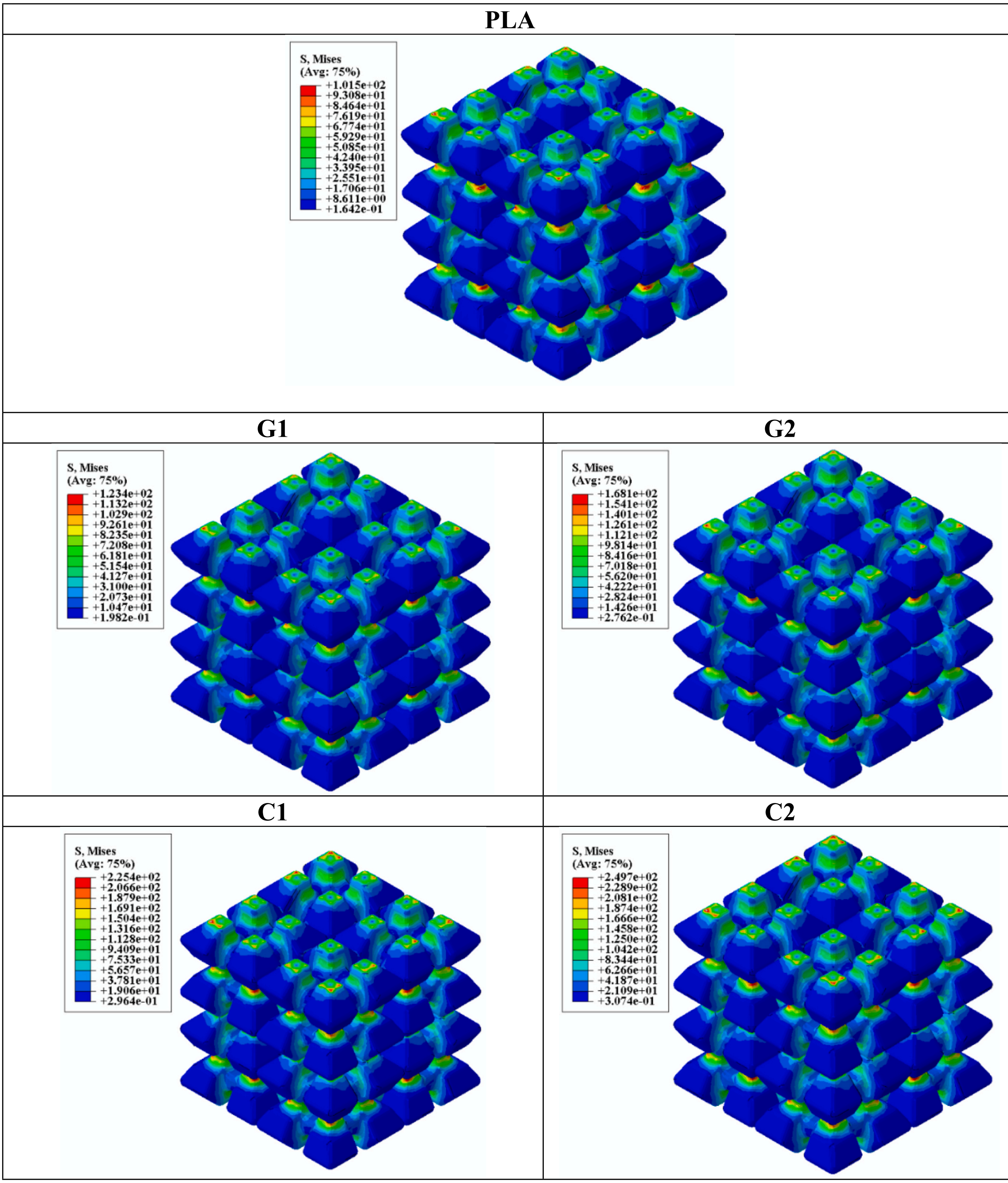

Fig. 8. Stress distribution of Cube structures, PLA, PLA/GO, and PLA/CNT.

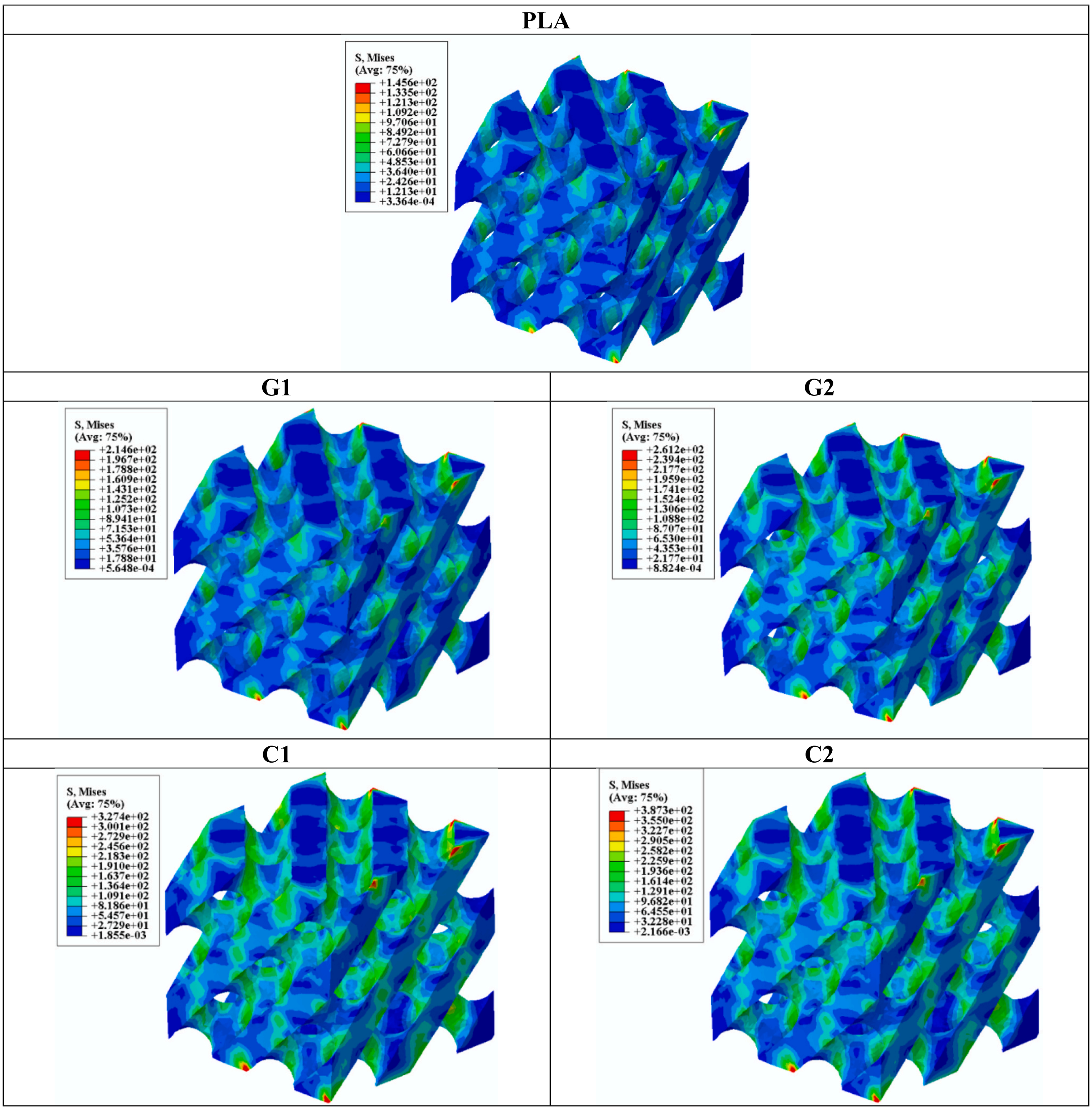

Fig. 9. Stress distribution of Diamond structure, PLA, PLA/GO, and PLA/CNT.

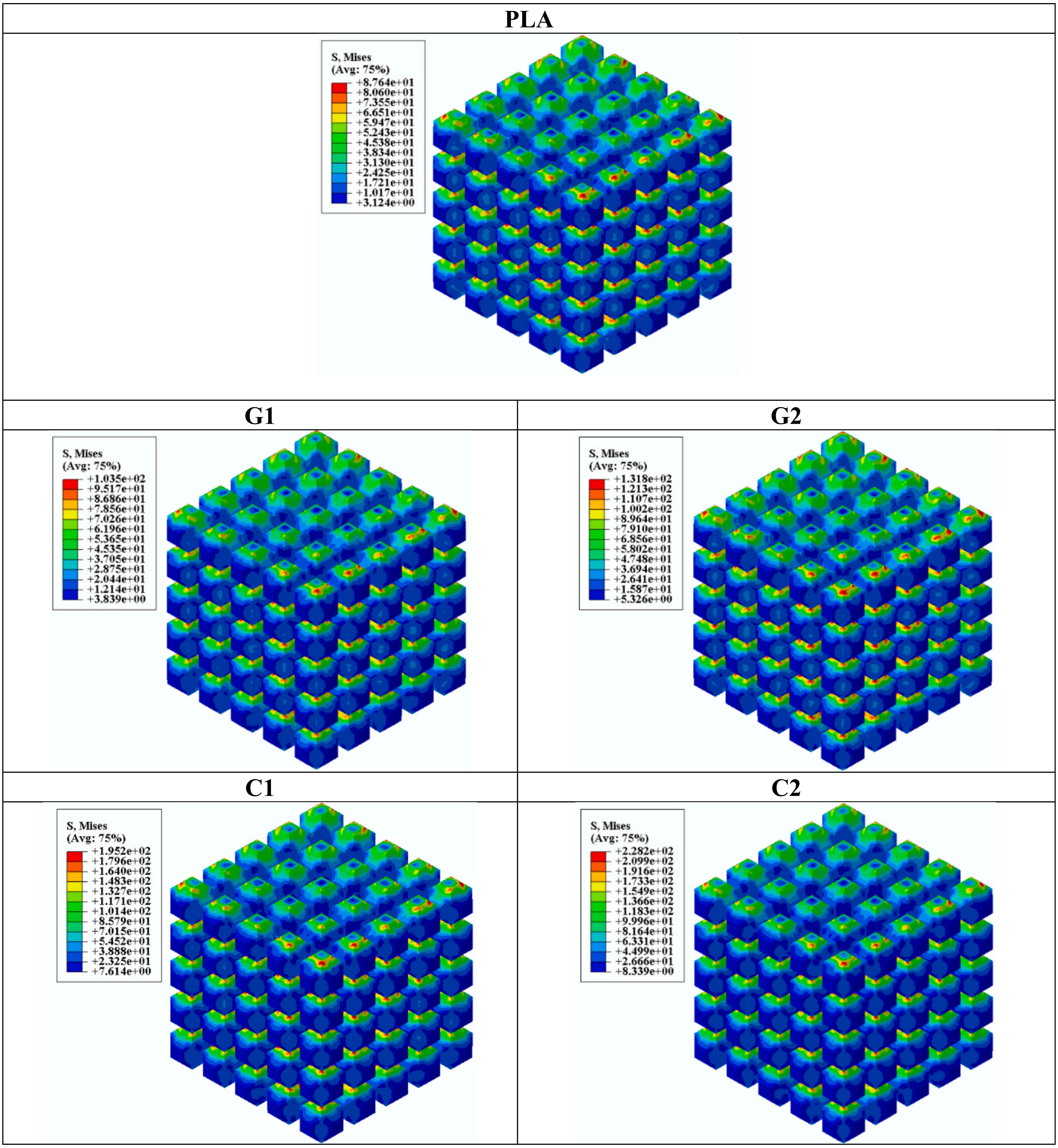

Fig. 10. Stress distribution of Lattice Diamond structure, PLA, PLA/GO, and PLA/CNT.

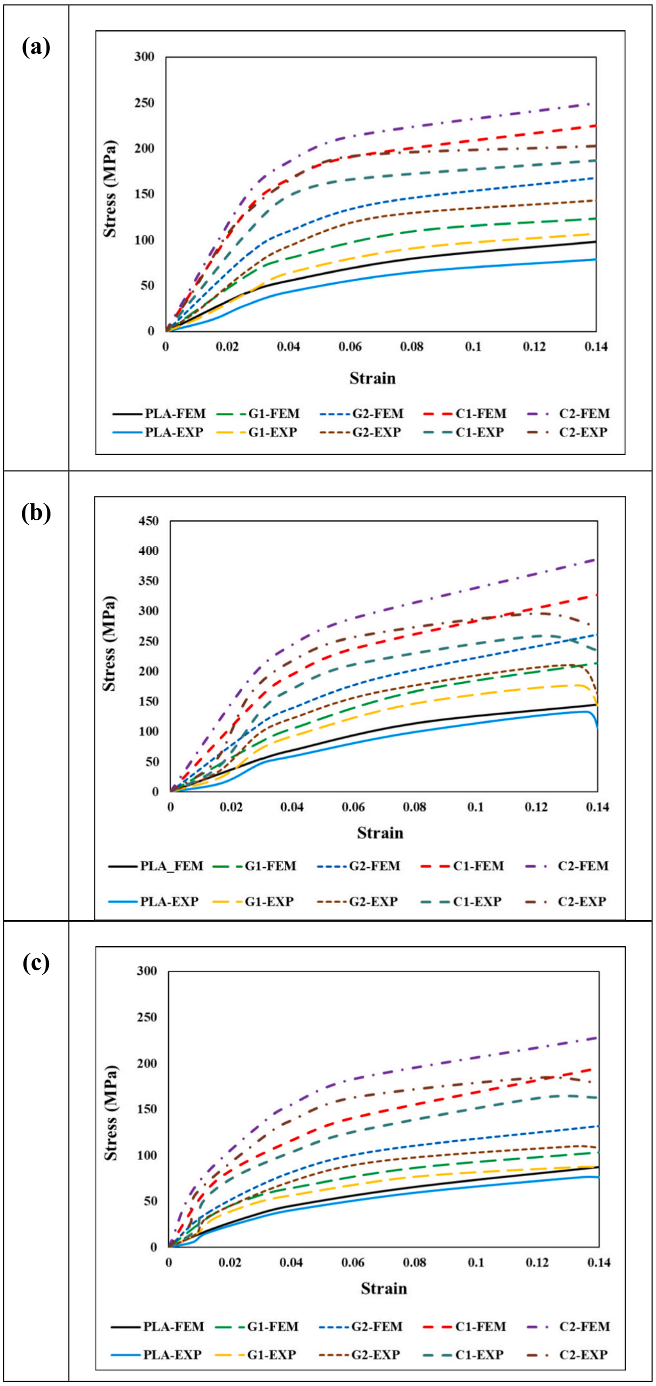

Fig. 11. Stress-Strain graph obtained by FEM and EXP for (a) Cube structure, (b) Diamond structure, and (c) Lattice Diamond structure.

Experimental results also showed an increase in elastic modulus for PLA/GO, from 1338.12 MPa (G1) to 1824.78 MPa (G2). Likewise, PLA/CNT's modulus rose from 3885.75 MPa (C1) to 4287.22 MPa (C2). However, the mechanical performance significantly declined for G3 and C3, as confirmed by the experimental results.

The mechanical behavior of the additive manufactured scaffolds (Cube, Diamond, and Lattice Diamond) was analyzed using FEM under compressive testing, based on the mechanical properties of the additive manufactured nanocomposites under experimental study. The scaffolds' behavior was evaluated using the Mooney-Rivlin hyperelastic model, as outlined in Section 3. The Mooney-Rivlin constants applied in the finite element simulations are provided in Table 2.

Figs. 8-10 show the stress distribution for the Cube, Diamond, and Lattice Diamond scaffolds, respectively. The Diamond scaffold exhibited superior mechanical performance compared to the Cube and Lattice Diamond scaffolds. From Fig. 8, the maximum stress was concentrated in the links, causing failure initiation in these areas, which agrees with the experimental findings. Fig. 9 shows that the stress was uniformly distributed throughout the Diamond structure, resulting in fracture patterns consistent with the experimental results. Fig. 10 demonstrates that maximum stress was on the areas in which Lattice Diamond's cells were in contact.

Fig. 11 illustrates the stress–strain curves of cube, diamond, and lattice diamond scaffolds from the FEMs. Compared to scaffolds made from PLA/GO and PLA reinforced with 0.2 wt% CNT, those fabricated with PLA reinforced with 0.4 wt% CNT exhibited enhanced mechanical performance across all scaffold topologies. The compressive strengths of the cube, diamond, and lattice diamond scaffolds were measured at 249.7 MPa, 387.29 MPa, and 228.2 MPa, respectively, for those made with PLA/0.4 wt% CNT. Notably, the diamond scaffold exhibited superior mechanical properties compared to the cube and lattice diamond structures. Fig. 11 indicates that the deviation observed in the PLA and PLA/GO scaffolds is less than that in the PLA/CNT scaffolds. The formation of CNT within the scaffolds' links significantly influences the mechanical performance of the scaffolds due to the potential for localized weakness in areas with CNT agglomeration. The dispersion level of CNT within the 3D-printed scaffolds exhibited greater sensitivity. As a result, when damage was observed in PLA/CNT scaffolds during a compressive test, the measured stress was lower than that predicted by ideal finite element simulations. As shown in Fig. 11, the difference between the FEM and EXP results at the beginning stage of EXP stress–strain curves in the Diamond and Lattice Diamond structures is related to the contact between the scaffolds and the upper fixture. This is because the upper fixture surface partially touched these scaffolds' top surface at the beginning, therefore the initial stress–strain slope is lower at the beginning.

Table 3 presents the elastic modulus and compressive strength of additive manufactured scaffolds obtained through FEM and experimental measurements. Across all configurations, the elastic modulus of the diamond scaffolds exceeded that of both the cube and lattice diamond scaffolds. Furthermore, the results indicate a satisfactory degree of agreement between the elastic modulus values derived from the experimental procedure and those obtained through FEM, with deviations ranging from 11.5 % to 23 % depending on the filament and scaffold topology. Moreover, the compressive strength of structures reported by FEM and EXP has acceptable deviation between 8.54 % to 28.74 %.

To assess the impact of mechanical improvements and structural architecture on vibrational response, the natural frequencies across five successive modes were identified using FEM. This was achieved through frequency simulation using the Lanczos Eigensolver. The natural frequencies and modes of the investigated scaffolds are shown in Fig. 12 and reported in Table 4. As mechanical properties improve in the modified filaments, the natural frequency value increases significantly. For example, an 86 % rise can be observed in the Cube structure's 5th mode, from 6932.6 Hz to 12951 Hz. Diamond and Lattice Diamond scaffolds exhibit higher frequencies than Cube scaffolds. For Cube and Diamond scaffolds, the frequencies across five modes were relatively close, with variations ranging from 2802 Hz (PLA) to 5187.7 Hz (C2) for Cube, and from 4604 Hz (PLA) to 8745 Hz (C2) for Diamond. In contrast, Lattice Diamond scaffolds showed a broader frequency variation, from 9161.3 Hz (PLA) to 17089 Hz (C2). This wider frequency range may limit the application scope of Lattice Diamond scaffolds compared to Cube and Diamond scaffolds.

5. Conclusion

This study evaluates AM PLA nanocomposite scaffolds by investigating the effect of architecture and modified PLA filaments on their

Table 3
Compressive strength and elastic modulus additive manufactured scaffolds.

Scaffold	Inclusion	Compressive strength (MPa)			Elastic modulus (MPa)		
		FEM	EXP	Error (%)	FEM	EXP	Error (%)
Cube	PLA	98.53	78.95	19.87	1769.26	1565.26	11.53
	G1	123.42	107.04	13.27	2005.92	1697.41	15.38
	G2	168.13	143.30	14.77	2749.41	2274.57	17.27
	C1	225.46	187.08	17.02	4165.26	3472.98	16.62
	C2	249.73	203.08	18.68	4635.55	3721.88	19.71
Diamond	PLA	145.60	133.17	8.54	2488.46	2233.14	10.26
	G1	214.58	177.26	17.39	2742.69	2291.24	16.46
	G2	261.17	211.12	19.16	3489	2814.58	19.33
	C1	327.40	259.39	20.77	5927.73	4840.58	18.34
	C2	387.29	275.98	28.74	6626.28	5114.83	22.81
Lattice Diamond	PLA	87.64	76.14	13.12	1783.74	1559.17	12.59
	G1	103.47	87.63	15.31	2016.59	1731.24	14.15
	G2	131.80	110.06	16.49	2741.02	2306.57	15.85
	C1	195.23	162.63	16.70	3919.89	3295.06	15.94
	C2	228.20	184.56	19.12	4392.64	3487.32	20.61

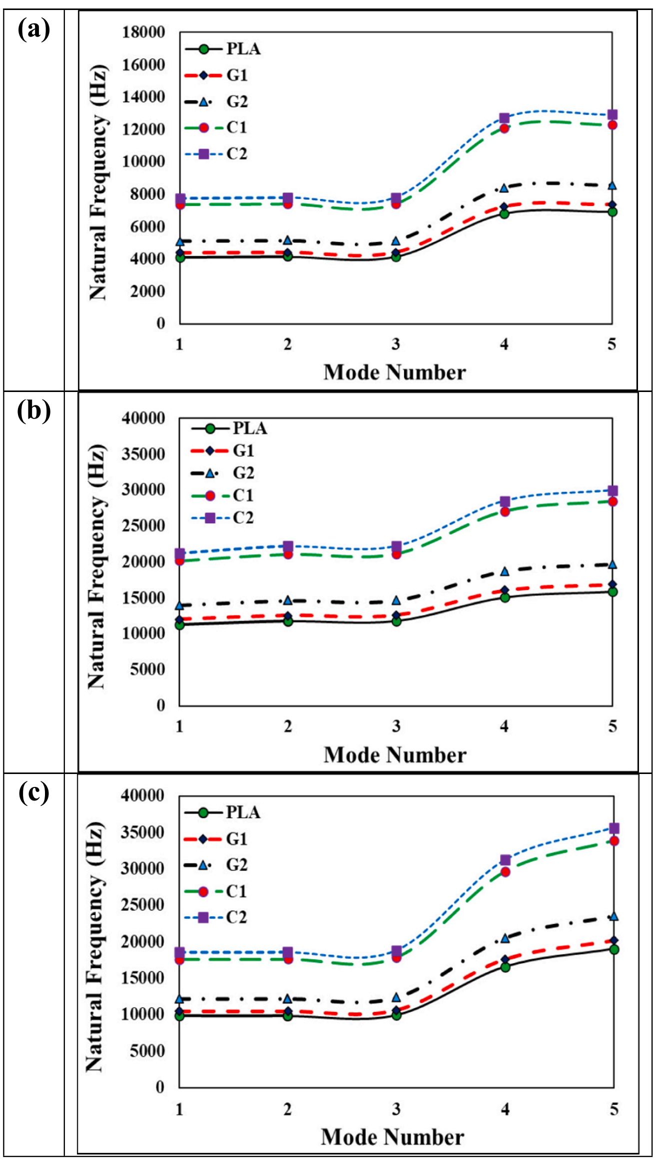

Fig. 12. The natural frequency of (a) Cube structure, (b) Diamond structure, and (c) Lattice Diamond structure.

Table 4
The natural frequency of structures in 5 successive modes.

Cube Structure Natural Frequency (Hz)					
Mode	*1st*	*2nd*	*3rd*	*4th*	*5th*
PLA	4130.6	4154.5	4161.9	6803.4	6932.6
G1	4393	4418	4426	7232.6	7370.5
G2	5116	5143.9	5153.4	8414.7	8575.1
C1	7381.5	7414.8	7429	12,114	12,324
C2	7763.3	7796.9	7811.9	12,737	12,951
Diamond Structure Natural Frequency (Hz)					
Mode	*1st*	*2nd*	*3rd*	*4th*	*5th*
PLA	11,306	11,803	11,843	15,111	15,910
G1	12,027	12,556	12,599	16,078	16,927
G2	14,011	14,631	14,680	18,744	19,730
C1	20,207	21,118	21,189	27,113	28,513
C2	21,247	22,209	22,284	28,525	29,992
Lattice Diamond Structure Natural Frequency (Hz)					
Mode	*1st*	*2nd*	*3rd*	*4th*	*5th*
PLA	9856.7	9859.1	9994.6	16,586	19,018
G1	10,483	10,486	10,630	17,641	20,223
G2	12,210	12,214	12,385	20,549	23,542
C1	17,639	17,647	17,910	29,685	33,906
C2	18,557	18,565	18,847	31,229	35,646

mechanical properties and vibrational behavior. Using PLA reinforced with GO and CNT, three scaffold topologies—Cube, Diamond, and Lattice Diamond—were fabricated and evaluated under compression. Moreover, the possibility of fabricating test samples with modified PLA filaments was evaluated and their mechanical properties were predicted using experimentally validated micromechanics modelling. FESEM analysis revealed uniform dispersion of nanomaterials at 0.2 wt% and 0.4 wt%, while 0.6 wt% led to agglomerations, negatively impacting mechanical performance. Compressive tests measured elastic modulus and compressive strength, and the results were compared with FEM. To predict the impact of agglomeration inside the PLA matrix, agglomeration formation was also studied. RVE models, analyzed under PBC, showed a deviation of 11.5 % to 23 % from experimental data, confirming their accuracy. The Mooney-Rivlin material behavior was considered for scaffold simulations by determining its constants from the experimental tests conducted on samples that were 3D-printed. Both experimental and FEM results indicated that the Diamond scaffold, reinforced with 0.4 wt% CNT, exhibited superior mechanical properties, with a compressive strength of 387.29 MPa compared to 249.7 MPa for the Cube and 228.2 MPa for the Lattice Diamond. Thus, the Diamond scaffold with 0.4 wt% CNT was identified as the optimal design for enhanced mechanical performance. The vibrational response shows that the reinforced scaffolds showed higher natural frequencies. In addition, Cube and Diamond scaffolds have closer natural frequencies across five modes compared to Lattice Diamond scaffolds. The variation in frequency behavior should be considered in the design, as it increases the risk of reaching resonance, potentially limiting their use.

CRediT authorship contribution statement

Sajad Niazi Angili: Writing – original draft, Project administration, Methodology, Investigation, Formal analysis, Conceptualization. **Mohammadreza Morovvati:** Writing – review & editing, Supervision, Conceptualization. **Yashar Vatandoust:** Writing – original draft, Methodology, Formal analysis. **Mohammad Fotouhi:** Investigation, Writing – review & editing. **Mahdi Bodaghi:** Investigation, Writing – review & editing.

Declaration of competing interest

The authors declare that they have no known competing financial interests or personal relationships that could have appeared to influence the work reported in this paper.

Data availability

Data will be made available on request.

References

[1] Attaran M. The rise of 3-D printing: The advantages of additive manufacturing over traditional manufacturing. Bus Horiz 2017;60(5):677–88.
[2] Coffigniez M, Laurent Gremillard S, Balvay J, Lachambre JA, Boulnat X. Direct-ink writing of strong and biocompatible titanium scaffolds with bimodal interconnected porosity. Addit Manuf 2021;39:101859.
[3] Zhu Wei, Qu Xin, Zhu Jie, Ma Xuanyi, Patel Sherrina, Liu Justin, Wang Pengrui et al. Direct 3D bioprinting of prevascularized tissue constructs with complex microarchitecture, Biomaterials 124 (2017) 106-115.
[4] Cui W, Yang Y, Di L, Dababneh F. Additive manufacturing-enabled supply chain: Modeling and case studies on local, integrated production-inventory-transportation structure. Addit Manuf 2021;48:102471.
[5] Lucarini S, Hossain M, Garcia-Gonzalez D. Recent advances in hard-magnetic soft composites: synthesis, characterisation, computational modelling, and applications. Compos Struct 2022;279:114800.
[6] ul Haq Muhammad Rizwan, Nazir Aamer, Lin Shang-Chih, Jeng Jeng-Ywan. Design and performance evaluation of multifunctional midsole using functionally gradient wave springs produced using multijet fusion additive manufacturing process. Mater Today Commun 2022;31:103505.
[7] Putra NE, Moosabeiki V, Leeflang MA, Zhou J, Zadpoor AA. Biodegradation-affected fatigue behavior of extrusion-based additively manufactured porous iron–manganese scaffolds. Acta Biomater 2024;178:340–51.
[8] Lakhdar Y, Tuck C, Binner J, Terry A, Goodridge R. Additive manufacturing of advanced ceramic materials. Prog Mater Sci 2021;116:100736.
[9] Stepinac L, Galić J, Vassilopoulos AP. Experimental and numerical investigation of an additively manufactured sandwich composite bridge deck utilizing gyroid building blocks. Compos Struct 2024;343:118304.
[10] Wang B, Ming Y, Zhu Y, Yao X, Ziegmann G, Xiao H, et al. Fabrication of continuous carbon fiber mesh for lightning protection of large-scale wind-turbine blade by electron beam cured printing. Addit Manuf 2020;31:100967.
[11] Wang Y, Zhou Y, Lin L, Corker J, Fan M. Overview of 3D additive manufacturing (AM) and corresponding AM composites. Compos A Appl Sci Manuf 2020;139:106114.
[12] Tymrak BM, Kreiger M, Pearce JM. Mechanical properties of components fabricated with open-source 3-D printers under realistic environmental conditions. Mater Des 2014;58:242–6.
[13] Sun Q, Rizvi GM, Bellehumeur CT, Gu P. Effect of processing conditions on the bonding quality of FDM polymer filaments. Rapid Prototyp J 2008;14(2):72–80.
[14] Song X, Weng Y, Zhirui Ma Yu, Han XZ, Zhang C. Sustainable improvement in the polylactic acid properties of 3D printing filaments: The role of bamboo fiber and epoxidized soybean oil-branched cardanol ether compatibilizer. Polym Compos 2024.
[15] Jamadar IM, Kamate P, Samal PK. Evaluation of fatigue characteristics of 3D printed/composites reinforced with carbon fiber using design of experiments. Polym Compos 2024.
[16] Caulfield B, McHugh PE, Lohfeld S. Dependence of mechanical properties of polyamide components on build parameters in the SLS process. J Mater Process Technol 2007;182(1–3):477–88.
[17] Gu H, Ma C, Junwei Gu, Guo J, Yan X, Huang J, et al. An overview of multifunctional epoxy nanocomposites. J Mater Chem C 2016;4(25):5890–906.
[18] Gu J, Yang X, Lv Z, Li N, Liang C, Zhang Q. Functionalized graphite nanoplatelets/epoxy resin nanocomposites with high thermal conductivity. Int J Heat Mass Transf 2016;92:15–22.
[19] Dou J, Zhang Q, Ma M, Junwei Gu. Fast fabrication of epoxy-functionalized magnetic polymer core-shell microspheres using glycidyl methacrylate as monomer via photo-initiated miniemulsion polymerization. J Magn Magn Mater 2012;324(19):3078–82.
[20] Angili Sajad Niazi, Reza Morovvati Mohammad, Kardan-Halvaei Mostafa, Saber-Samandari Saeed, Razmjooee Kavoos, Abed Azher M, Toghraie Davood, Khandan Amirsalar. Fabrication and finite element simulation of antibacterial 3D printed Poly L-lactic acid scaffolds coated with alginate/magnesium oxide for bone tissue regeneration. Int J Biol Macromol 2023;224:1152–1165.
[21] Kardan-Halvaei M, Morovvati MR, Niazi Angili S, Saber-Samandari S, Razmjooee K, Toghraie D, et al. Fabrication of 3D-printed hydroxyapatite using freeze-drying method for bone regeneration: RVE and finite element simulation analysis. J Mater Res Technol 2023;24:8682–92.
[22] Rouf, Saquib, Raina Ankush, Ul Haq Mir Irfan, Naveed Nida, Jeganmohan Sudhanraj, Farzana Kichloo Aysha. 3D printed parts and mechanical properties: Influencing parameters, sustainability aspects, global market scenario, challenges and applications. Adv Ind Eng Polym Res 5, no. 2022;3:143–158.
[23] Wang Wenzhao, Zhang Boqing, Li Mingxin, Li Jun, Zhang Chengyun, Han Yanlong, Wang Li et al. 3D printing of PLA/n-HA composite scaffolds with customized mechanical properties and biological functions for bone tissue engineering. Compos Part B: Eng 2021;224: 109192.
[24] Harun WSW, Kamariah MSIN, Norhamidi Muhamad SAC, Ghani FA, Mohamed Z. A review of powder additive manufacturing processes for metallic biomaterials. Powder Technol 2018;327:128–51.
[25] Hu LL, Zh Zhou M, Deng H. Dynamic indentation of auxetic and non-auxetic honeycombs under large deformation. Compos Struct 2019;207:323–30.
[26] Gibson Lorna J, Michael F. Ashby, Brendan A. Harley. Cellular materials in nature and medicine. Cambridge University Press; 2010.
[27] Zhao W, Yue C, Liu L, Leng J, Liu Y. Mechanical behavior analyses of 4D printed metamaterials structures with excellent energy absorption ability. Compos Struct 2023;304:116360.
[28] Zhan C, Li M, McCoy R, Zhao L, Weiyi Lu. 3D printed hierarchical re-entrant honeycombs: enhanced mechanical properties and the underlying deformation mechanisms. Compos Struct 2022;290:115550.
[29] Zhao Y, Qianqian Wu, Zhao C, Zhou H, Linzhi Wu. Progress of structural scaffold biomaterials for bone tissue defect repair: a cutting-edge review. Compos Struct 2024:0263–8223.
[30] Wang X, Zhang L, Song Bo, Zhang J, Fan J, Zhang Z, et al. Anisotropic mechanical and mass-transport performance of Ti6Al4V plate-lattice scaffolds prepared by laser powder bed fusion. Acta Biomater 2022;148:374–88.
[31] Zhang L, Song Bo, Yang L, Shi Y. Tailored mechanical response and mass transport characteristic of selective laser melted porous metallic biomaterials for bone scaffolds. Acta Biomater 2020;112:298–315.
[32] Kolken HMA, Janbaz S, Leeflang SMA, Lietaert K, Weinans HH, Zadpoor AA. Rationally designed meta-implants: a combination of auxetic and conventional meta-biomaterials. Mater Horiz 2018;5(1):28–35.
[33] Li Z, Chen Z, Chen X, Zhao R. Design and evaluation of TPMS-inspired 3D-printed scaffolds for bone tissue engineering: enabling tailored mechanical and mass transport properties. Compos Struct 2024;327:117638.
[34] Liu Z, Gong He, Gao J, Liu Lu. Bio-inspired design, mechanical and mass-transport characterizations of orthotropic TPMS-based scaffold. Compos Struct 2023;321:117256.
[35] Xie H, Wang Y, Liu F, Tang Q, Chen J, Luo T, et al. Strengthening mechanism of TPMS interpenetrating phase composites for bone tissue engineering. Compos Struct 2024;118526.
[36] Xie H, Chen J, Liu F, Wang R, Tang Y, Wang Y, et al. Ti-PEEK interpenetrating phase composites with minimal surface for property enhancement of orthopedic implants. Compos Struct 2024;327:117689.
[37] Feng P, Jia J, Liu M, Peng S, Zhao Z, Shuai C. Degradation mechanisms and acceleration strategies of poly (lactic acid) scaffold for bone regeneration. Mater Des 2021;210:110066.
[38] Guo Wang, Liu Chao, Bu Wenlang, Yang Yanjuan, Guo Feng, Li Jiaqi, Wang Enyu et al. 3D printing of polylactic acid/boron nitride bone scaffolds: mechanical properties, biomineralization ability and cell responses. Ceram Int 2023;49(15):25886–25898.
[39] Murariu M, Dubois P. PLA composites: from production to properties. Adv Drug Deliv Rev 2016;107:17–46.
[40] Guo Wang, Yang Yanjuan, Liu Chao, Bu Wenlang, Guo Feng, Li Jiaqi, Wang Enyu et al. 3D printed TPMS structural PLA/GO scaffold: process parameter optimization, porous structure, mechanical and biological properties. J Mech Behav Biomed Mater 2023;142:105848.
[41] Scaffaro R, Lopresti F, Botta L, Rigogliuso S, Ghersi G. Integration of PCL and PLA in a monolithic porous scaffold for interface tissue engineering. J Mech Behav Biomed Mater 2016;63:303–13.
[42] Guo Wang, Mao Yufeng, Tang Xinru, Wang Enyu, Peng Ziying, Wu Yunlei, Zhang Mingzhi et al. Copper-loaded microporous chitosan generated within a 3D-Printed polylactic acid-pearl Scaffold: structure and performance. ACS Appl Polym Mater 2024;6(23):14505–14517.
[43] Sivakumar NK, Kaaviya J, Palaniyappan S, Rahaman M, Pandiaraj S. Tribological performance of the novel 3D printed PLA/Almond shell particles added PLA single gradient functionally graded material (SGFGM). Mater Today Commun 2024:109611.

[44] Zhao G, Liu H-Y, Cui X, Xusheng Du, Zhou H, Mai Y-W, et al. Tensile properties of 3D-printed CNT-SGF reinforced PLA composites. Compos Sci Technol 2022;230: 109333.
[45] Sang L, Han S, Li Z, Yang X, Hou W. Development of short basalt fiber reinforced polylactide composites and their feasible evaluation for 3D printing applications. Compos B Eng 2019;164:629–39.
[46] Jing M, Sui G, Zhao J, Zhang Q, Qiang Fu. Enhancing crystallization and mechanical properties of poly (lactic acid)/milled glass fiber composites via self-assembled nanoscale interfacial structures. Compos A Appl Sci Manuf 2019;117: 219–29.
[47] Thirugnanasamabandam A, Prabhu B, Varsha Mageswari V, Murugan KR, Kadirgama K. Wood flour/ceramic reinforced Polylactic Acid based 3D-printed functionally grade structural material for integrated engineering applications: a numerical and experimental characteristic investigation. Int J Lightweight Mater Manufact 2024.
[48] Bustillos J, Montero D, Nautiyal P, Loganathan A, Boesl B, Agarwal A. Integration of graphene in poly (lactic) acid by 3D printing to develop creep and wear-resistant hierarchical nanocomposites. Polym Compos 2018;39(11):3877–88.
[49] Bayer IS. Thermomechanical properties of polylactic acid-graphene composites: a state-of-the-art review for biomedical applications. Materials 2017;10(7):748.
[50] Gonçalves C, Gonçalves IC, Magalhães FD, Pinto AM. Poly (lactic acid) composites containing carbon-based nanomaterials: a review. Polymers 2017;9(7):269.
[51] Gonçalves Carolina, Artur Pinto, Ana Vera Machado, Joaquim Moreira, Inês C. Gonçalves, Fernao Magalhaes. Biocompatible reinforcement of poly (Lactic acid) with graphene nanoplatelets. Polym Compos 2018;39: E308-E320.
[52] Prashantha K, Roger F. Multifunctional properties of 3D printed poly (lactic acid)/ graphene nanocomposites by fused deposition modeling. J Macromol Sci A 2017; 54(1):24–9.
[53] Patti A, Lecocq H, Serghei A, Acierno D, Cassagnau P. The universal usefulness of stearic acid as surface modifier: applications to the polymer formulations and composite processing. J Ind Eng Chem 2021;96:1–33.
[54] Zhang Y, Ding C, Zhang Na, Chen C, Di X, Zhang Y. Surface modification of silica micro-powder by titanate coupling agent and its utilization in PVC based composite. Constr Build Mater 2021;307:124933.
[55] Ye X, Wang E, Huang Y, Yang Y, Zhang T, Hui You Yu, et al. Biomolecule-grafted GO enhanced the mechanical and biological properties of 3D printed PLA scaffolds with TPMS porous structure. J Mech Behav Biomed Mater 2024;157:106646.
[56] Pandey Atul, Singh Jasvinder, Singh Malkeet, Singh Gurjeet, Parmar Avanish Singh, Chaudhary Shilpi. Graphene oxide/polylactic acid composites with enhanced electrical and mechanical properties for 3D-printing materials. J Mol Struct (2025): 141420.
[57] Yohannan A, Vincent S, Divakaran N, Venugopal AKP, Patra S, Ashish K, et al. Experimental and simulation studies of hybrid MWCNT/montmorillonite reinforced FDM based PLA filaments with multifunctional properties enhancement. Polym Compos 2024;45(1):507–22.
[58] Rafiee R, Zehtabzadeh H, Amini MR. Predicting mechanical properties of 3D printed nanocomposites using multi-scale modeling. Addit Manuf 2024;83:104055.
[59] Sahoo Nanda Gopal, Rana Sravendra, Cho Jae Whan, Li Lin, Chan Siew Hwa. Polymer nanocomposites based on functionalized carbon nanotubes. Progr Polym Sci 2010;35(7): 837–867.
[60] Gao Qi, Ye X, He E, Yan T, Wang Y, Ye Y, et al. 3D printed fabrication of ultra-structured composites of carbonyl iron powder@ carbon@ carbon black/polylactic acid for efficient microwave absorption. Polym Compos 2024.
[61] Mai F, Habibi Y, Raquez J-M, Dubois P, Feller J-F, Peijs T, et al. Poly (lactic acid)/ carbon nanotube nanocomposites with integrated degradation sensing. Polymer 2013;54(25):6818–23.
[62] Kim Seong Yun, Shin Kook Seung, Lee Seung Hwan, Kim Kyeong Wung, Youn Jae Ryoun. Unique crystallization behavior of multi-walled carbon nanotube filled poly (lactic acid). Fib Polym 2010;11:1018–1023.
[63] García-Macías, Enrique, Guzmán Carlos Felipe, Saavedra Flores Erick I, Castro-Triguero Rafael. Multiscale modeling of the elastic moduli of CNT-reinforced polymers and fitting of efficiency parameters for the use of the extended rule-of-mixtures. Compos Part B: Eng 2019;159:114–131.
[64] Rossi M, Meo M. On the estimation of mechanical properties of single-walled carbon nanotubes by using a molecular-mechanics based FE approach. Compos Sci Technol 2009;69(9):1394–8.
[65] Morovvati MR, Niazi Angili S, Saber-Samandari S, Ghadiri Nejad M, Toghraie D, Khandan A. Global criterion optimization method for improving the porosity of porous scaffolds containing magnetic nanoparticles: Fabrication and finite element analysis. Mater Sci Eng B 2023;292:116414.
[66] Sun C-T, Vaidya RS. Prediction of composite properties from a representative volume element. Compos Sci Technol 1996;56(2):171–9.
[67] Hill R. Elastic properties of reinforced solids: some theoretical principles. J Mech Phys Solids 1963;11(5):357–72.
[68] Trzepieciński T, Ryzińska G, Gromada M, Biglar M. 3D microstructure-based modelling of the deformation behaviour of ceramic matrix composites. J Eur Ceram Soc 2018;38(8):2911–9.
[69] Hu Y, Jiafei Gu, Zhang Y, Liu G, Yi X, Liu X. FDM 3D printed MXene/recycled carbon fibre reinforced polylactic acid composites: interface optimization, toughening and enhanced electromagnetic shielding performance. Compos Commun 2024;101953.
[70] Siripongpreda T, Hoven VP, Narupai B, Rodthongkum N. Emerging 3D printing based on polymers and nanomaterial additives: Enhancement of properties and potential applications. Eur Polym J 2023;184:111806.
[71] Liang Li, Huang T, Songxiang Yu, Cao W, Tingting Xu. Study on 3D printed graphene/carbon fiber multi-scale reinforced PLA composites. Mater Lett 2021; 300:130173.
[72] Systèmes D 2016 Abaqus analysis User's Guide V2016.
[73] Imanian, Mohammad Ebrahim, Kardan-Halvaei, Mostafa, Nasrollahi, Fatemeh, Imanian, Ali, Montazerian, Hossein, Nasrollahi, Vahid. 3D printed flexible wearable sensors based on triply periodic minimal surface structures for biomonitoring applications. Smart Mater Struct 2022;32(1):015015.
[74] Afshar R, Jeanne S, Abali BE. Nonlinear material modeling for mechanical characterization of 3-D printed PLA polymer with different infill densities. Appl Compos Mater 2023;30(3):987–1001.